Targeting *de novo* lipogenesis improves gemcitabine efficacy in pancreatic ductal adenocarcinoma

Sarah E Hancock[1,2], Linda Garthwaite[1], Konstantina Harellis[1], Michael Susetio[1], Eileen Ding[2], Laura Choong[1,3], Osvaldo Contreras[3,4] Amy Nguyen[1], Josiah Lising[2], Felicia KM Hansen[5], Puttandon Wongsomboon[5], Jan Philipp Menzel[5], Berwyck LJ. Poad[5,6], Todd W Mitchell[7,8], Stephen J Blanksby[5,6] Nigel Turner[1,2,*]

[1]Cellular Bioenergetics Laboratory, Victor Chang Cardiac Research Institute, Darlinghurst, NSW, Australia

[2]Department of Pharmacology, School of Biomedical Sciences, UNSW Sydney, NSW, Australia.

[3]School of Clinical Medicine, Faculty of Medicine & Health, University of New South Wales, UNSW Sydney, Sydney, NSW, Australia

[4]Developmental and Regenerative Biology Division, Victor Chang Cardiac Research Institute, Darlinghurst, NSW, Australia

[5]School of Chemistry and Physics, Queensland University of Technology, Brisbane, QLD. Australia

[6]Central Analytical Research Facility, Queensland University of Technology, Brisbane, QLD, Australia

[7]School of Medical, Indigenous & Health Sciences, University of Wollongong, Wollongong, NSW, Australia

[8]Molecular Horizons, University of Wollongong, Wollongong, NSW, Australia

* Corresponding author. Email n.turner@victorchang.edu.au

22 **Abbreviations**

23 *ACC* acetyl-CoA carboxylase, *AMP*$^{+}$ *N*-(4-aminomethylphenyl)pyridinium, *BSA* bovine serum
24 albumin, *CE* cholesteryl ester, *Cer* ceramide, *CL* cardiolipin, *CombAT* combination therapy attenuated,
25 *CON* control, *DG* diacylglycerol, *ELOVL* elongation of very long chain fatty acid protein, *FADS2* fatty
26 acid desaturase 2, *FAS* fatty acid synthase, *FOLFIRINOX* folinic acid, 5-fluorouracil, irinotecan and
27 oxaliplatin; *GEMC* gemcitabine, *GEMR* gemcitabine resistant, IC_{50} half maximal inhibitory
28 concentration, *LC-MS* liquid chromatography-mass spectrometry, *LPC* lysophosphatidylcholine, *LPE*
29 lysophosphatidylethanolamine, *MUFA* monounsaturated fatty acid, *OzFAD* ozone-induced fatty acid
30 discovery, *PBS* phosphate buffered saline *PC* phosphatidylcholine, *PDAC* pancreatic ductal
31 adenocarcinoma, *PE* phosphatidylethanolamine, *PG* phosphatidylglycerol, *PS* phosphatidylserine, *PTX*
32 paclitaxel, *PUFA* polyunsaturated fatty acid, *SCD1* stearoyl-CoA desaturase 1, *SFA* saturated fatty acid,
33 *siRNA* small interfering siRNA *SM* sphingomyelin, *TBST* Tris-buffered saline with 0.1% Tween20, *TG*
34 triacylglycerol, *VEH* vehicle.

Abstract

Pancreatic ductal adenocarcinoma (PDAC) is a highly aggressive disease with few treatment options and poor survivability. In this work we sought to characterise metabolic adaptations to gemcitabine (GEMC)-based chemotherapy exposure to discover new therapeutic targets for improving treatment efficacy. We show that GEMC resistance (GEMR) upregulates *de novo* lipogenesis in Panc1 and MiaPaCa2 cells through increased activity and expression of acetyl-CoA carboxylase (ACC), fatty acid synthase (FAS) and stearoyl-CoA desaturase 1 (SCD1). We also discovered alternate fatty acid desaturase 2 (FADS2) activity in Panc1 cells, which led to the production of sapienic acid (FA 16:1*n*-10, *cis*) from palmitic acid (FA 16:0). Knockdown of key lipid synthesis enzymes sensitised cells to GEMC treatment, with FAS (both cell lines), SCD1 (MiaPaCa2 only) and SCD1+FADS2 (Panc1) knockdown showing the greatest reduction in cell growth when combined with GEMC treatment. In Panc1 cells, both desaturases upregulated their activity when the alternate was knocked down, necessitating the need for dual desaturase knockdown in this cell line. PDAC cells attenuated to grow in combination GEMC/paclitaxel (CombAT) also displayed enhanced *de novo* lipogenesis; however, combination chemotherapy significantly downregulated FADS2 expression and activity in Panc1 CombAT cells rendering them more sensitive to SCD1 knockdown. We conclude that co-targeting lipid synthesis in PDAC could be a viable strategy for improving the efficacy of both GEMC monotherapy and combination GEMC/PTX therapy.

53 ## Introduction

54 Pancreatic ductal adenocarcinoma (PDAC) is the twelfth most common cancer worldwide, with close
55 to half a million new cases being diagnosed in 2020 [1]. Despite its relatively low incidence rate, the
56 mortality associated with PDAC remains high, with a global 5-year overall survival rate of just 9% [2].
57 The ongoing poor survivability of PDAC is a result of many contributing factors. PDAC is a highly
58 asymptomatic disease that is often detected at later stages, with fewer than 20% of cases being eligible
59 for surgical resection at the time of diagnosis [3]. For most patients only palliative chemotherapy remains
60 as a treatment option. Either FOLFIRINOX (folinic acid, 5-fluorouracil, irinotecan and oxaliplatin) or
61 gemcitabine (GEMC) monotherapy have long been the primary chemotherapy options for PDAC, with
62 the former coming at a cost of higher toxicity [4,5]. More recently, GEMC combined with albumin-bound
63 (nab-)paclitaxel (also known as Abraxane) has replaced GEMC monotherapy as the standard of care
64 for metastatic PDAC, but survivability still remains extremely poor with an increase in median overall
65 survival of only a few months when compared with GEMC monotherapy [6].

66 Underlying the poor treatability and chemoresistance of PDAC are a myriad of genetic mutations, many
67 of which are sporadic and heterogeneous between patients. Activating mutations in *KRAS* are common
68 and present in around 90% of tumours, as are inactivating mutations in *TP53*, *CDKN2A*, and *SMAD4*
69 (>20% of tumours) [3,7]. Beyond this, common mutations seen across PDAC tumours drop to <10% [3,8],
70 precluding the identification of druggable gene therapy targets that can impact a majority of patients.
71 The genetic mutations present in PDAC have wide-ranging impacts on tumour molecular biology,
72 activating diverse pro-survival and anti-apoptotic signalling pathways [9–11]. Further compounding the
73 chemoresistant nature of PDAC is the presence of a dense desmoplastic stroma that creates a hypoxic
74 tumour microenvironment and impedes the delivery of chemotherapy to cancer cells [12]. Together this
75 results in extensive metabolic reprogramming in PDAC to facilitate the acquisition of biomolecules
76 necessary to support cancer cell rapid growth and proliferation. Despite the lack of a good genetic
77 therapeutic target in PDAC, mutational effects likely converge on relatively fewer metabolic pathways
78 [13,14], making metabolism-based therapies an attractive pathway for improving options for PDAC
79 treatment.

80 The role of lipid metabolism in cancer cell survival, metastasis, and chemoresistance has become a
81 recent topic of interest across many different cancer types including PDAC [15–21]. Key *de novo*
82 lipogenesis enzymes are commonly upregulated in many cancers, consistent with the continual need for
83 accrual of lipids in cancer [22]. For example, fatty acid synthase (FAS) is the rate-limiting step in fatty
84 acid synthesis and catalyses the elongation of malonyl-CoA produced by acetyl-CoA carboxylase
85 (ACC) to palmitic acid (*i.e.*, FA 16:0, a fatty acid with 16 carbons and no carbon-carbon double bonds).
86 FAS is commonly expressed at high levels in a variety of cancers (reviewed by [23–25]), where its
87 overexpression often correlates to poorer survival [17,26] and chemotherapy resistance [17,27–29]. Aberrant

88 lipid metabolism is an emerging metabolic hallmark of PDAC, where fatty acid and sterol metabolism
89 is upregulated [18,30], and distinct lipid signatures can predict patient prognosis and resistance to
90 chemotherapy [15]. Collectively, relatively little is known about the role of lipid metabolism in PDAC
91 growth, metastasis, and chemoresistance, and a more complete elucidation of implicated metabolic
92 pathways could lead to the identification of novel therapeutic targets to improve PDAC treatment and
93 patient survival.

94 In this work, we describe significant increases in *de novo* lipogenesis following chronic treatment of
95 PDAC cells with GEMC monotherapy or combination GEMC/paclitaxel (PTX) therapy. We show that
96 targeting key lipogenic enzymes can improve the efficacy of GEMC chemotherapy, including ACC1,
97 FAS, stearoyl-CoA desaturase 1 (SCD1) and fatty acid desaturase 2 (FADS2). Furthermore, we describe
98 Δ6 desaturation of saturated fatty acids by FADS2 in PDAC for the first time, alongside selective
99 downregulation of FADS2 by chronic GEMC/PTX treatment offering a novel pathway towards dual
100 desaturase targeting to improve GEMC-based chemotherapy efficacy in PDAC.

101 # Results

102 ## Development of GEMR PDAC cell lines

103 Panc1 and MiaPaCa2 were chosen as model cell lines to explore chemotherapy-induced metabolic
104 reprogramming due to their divergent mutational heterogeneity (Figure S1 & Table S1) combined with
105 discrete metabolic phenotypes [31]. GEMR cells lines from Panc1 and MiaPaCa2 cells were developed as
106 described in Materials and methods, with the final concentration of GEMC for Panc1 cells being 150
107 nM and 64 nM for MiaPaCa2 cells. At these doses, Panc1 GEMR cells had an IC_{50} that was >2.5 times
108 that of CON cells (Table 1), and MiaPaCa2 GEMR IC_{50} was ~3 times that of CON. Few overt
109 morphological changes could be observed between GEMR and CON in either cell line (Figure S2).
110 Together these data suggest that both PDAC cell lines are newly adapted to GEMC, lacking the extreme
111 changes in cell morphology seen in more advanced GEMR PDAC models [32–34].

112 **Table 1:** half-maximal inhibitory concentration of control and gemcitabine-resistant (GEMR) PDAC
113 cell lines.

Cell line	IC_{50} (nM)	95% CI (nM)	p value*
Panc1 CON	273.3	136.0 - 575.5	-
Panc1 GEMR	720.5	427.2 - 1225.0	0.012
MiaPaCa2 CON	30.6	20.3 - 46.1	-
MiaPaCa2 GEMR	92.2	59.7 - 142.2	<0.001

114 *CON* control *GEMR* gemcitabine resistant IC_{50} half-maximal inhibitory concentration.
115 * control vs GEMR, non-linear regression with extra sum-of-squares F test, n= 3.
116

117 **GEMR alters lipid profile and increases lipid droplet number in Panc1 cells**

118 Previous work had indicated a distinct lipidomic signature associated with chemoresistant PDAC [15]. To
119 better understand impact of GEMR on PDAC cell lipid metabolism we performed untargeted
120 lipidomics. Untargeted lipidomics enabled the quantification of more than 400 distinct molecular lipid
121 species within Panc1 & MiaPaCa2 control & GEMR cells from 12 different classes of lipid, with 77
122 molecular species being differentially abundant between Panc1 control and GEMR cells (Figure 1A)
123 and 79 between MiaPaCa2 cell lines (Figure 1B). Roughly equal proportions of increased and decreased
124 lipid species were detected between Panc1 CON & GEMR cells (Figure 1A), while lipid species in
125 MiaPaCa2 GEMR cells were mostly decreased with GEMR (Figure 1B). Interestingly, Panc1 cells
126 appeared to have an overrepresentation of lipids containing saturated (no carbon-carbon double bonds;
127 SFA) or monounsaturated fatty acids (1 carbon-carbon double bond; MUFA) that were increased with
128 GEMR (Figure 1A), strongly suggesting the upregulation of *de novo* lipid synthesis within this cell line.
129 Confocal imaging of BODIPY-stained cells revealed increased lipid droplet number per cell in Panc1
130 GEMR cells when compared with CON, with no change in lipid droplet size (Figure 1D). No significant
131 change in lipid droplet number or size was observed between MiaPaCa2 CON and GEMR cells (Figure
132 1E); however, MiaPaCa2 CON cells contained approximately three times more neutral lipid droplets
133 per cell compared with Panc1 CON (Figure 1F). Together these data suggest a role for GEMC-driven
134 upregulation of *de novo* lipogenesis and lipid droplet biogenesis in Panc1 cells specifically.

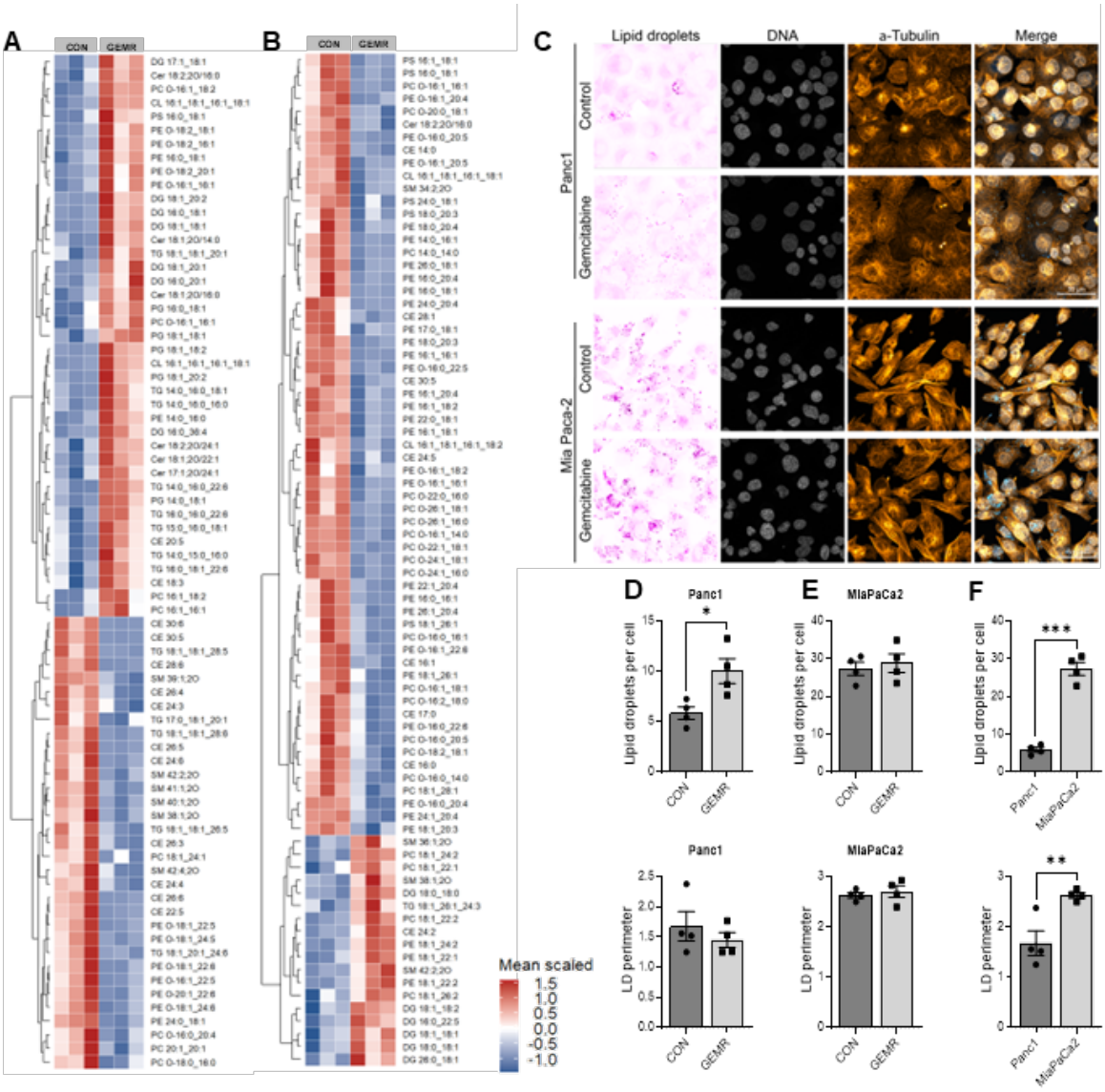

Figure 1: Differentially abundant lipid species from **A** Panc1 and **B** MiaPaCa2 control (CON) & gemcitabine-resitant (GEMR) cell lines detected by untargeted lipidomics (unpaired t test, $P < 0.05$). Lipids were quantified from internal standards, and values are mean-scaled. **C** Representative confocal images of BOPIDY-stained Panc1 & MiaPaCa2 CON & GEMR cells lines, with (**D-E**) quantification of lipid droplets per cell and lipid droplet perimeter (µm). **F** Comparison of lipid droplet number and size between Panc1 and MiaPaCa2 cells. Statistical significance was determined by unpaired t test, *$P < 0.05$ ** $P < 0.01$. *** $P < 0.001$. *CE* cholesteryl ester, *Cer* ceramide, *CL* cardiolipin, *DG* diacylglycerol, *LPC* lysophosphatidylcholine, *LPE* lysophosphatidylethanolamine, *PC* phosphatidylcholine, *PE* phosphatidylethanolamine, *PG* phosphatidylglycerol, *PS* phosphatidylserine, *SM* sphingomyelin, *TG* triacylglycerol

GEMR increases *de novo* lipogenesis in PDAC cell lines

To better understand GEMR-driven reprogramming of PDAC lipid metabolism we undertook extensive profiling of lipid synthesis pathways in both cell lines (Figure 2A). We measured *de novo* lipogenesis in PDAC cells by tracing the incorporation of radiolabelled glucose into the lipid fraction of both Panc1 and MiaPaCa2 CON & GEMR cells (Figure 2B). Surprisingly GEMR increased *de novo* synthesis of

151 lipid from glucose in both PDAC cell lines. To further elucidate specific changes in lipid metabolism
152 we next performed immunoblotting to characterise changes in total and activated enzymes involved in
153 lipid synthesis. Phosphorylation of acetyl-CoA carboxylase 1 (ACC1) at serine 79 was decreased in
154 Panc1 GEMR (indicating enhanced activity of this enzyme) alongside an increased abundance of fatty
155 acid synthase (FAS, Figure 2C). MiaPaCa2 GEMR cells had increased total ACC compared to CON
156 (Figure 2D). Together, these data suggest that GEMR upregulates *de novo* lipogenesis in both PDAC
157 cell lines.

158 Given the upregulation of lipid synthesis with GEMR in both cell lines we also assessed the impact of
159 GEMR on fatty acid oxidation (FAO) using radiolabelled palmitate. We found increased FAO in Panc1
160 GEMR cell lines and minimal amounts of FAO in both CON and GEMR MiaPaCa2 cells (Figure S3A).
161 No change was observed with GEMR in either cell line for radiolabelled palmitic acid uptake (Figure
162 S3B).

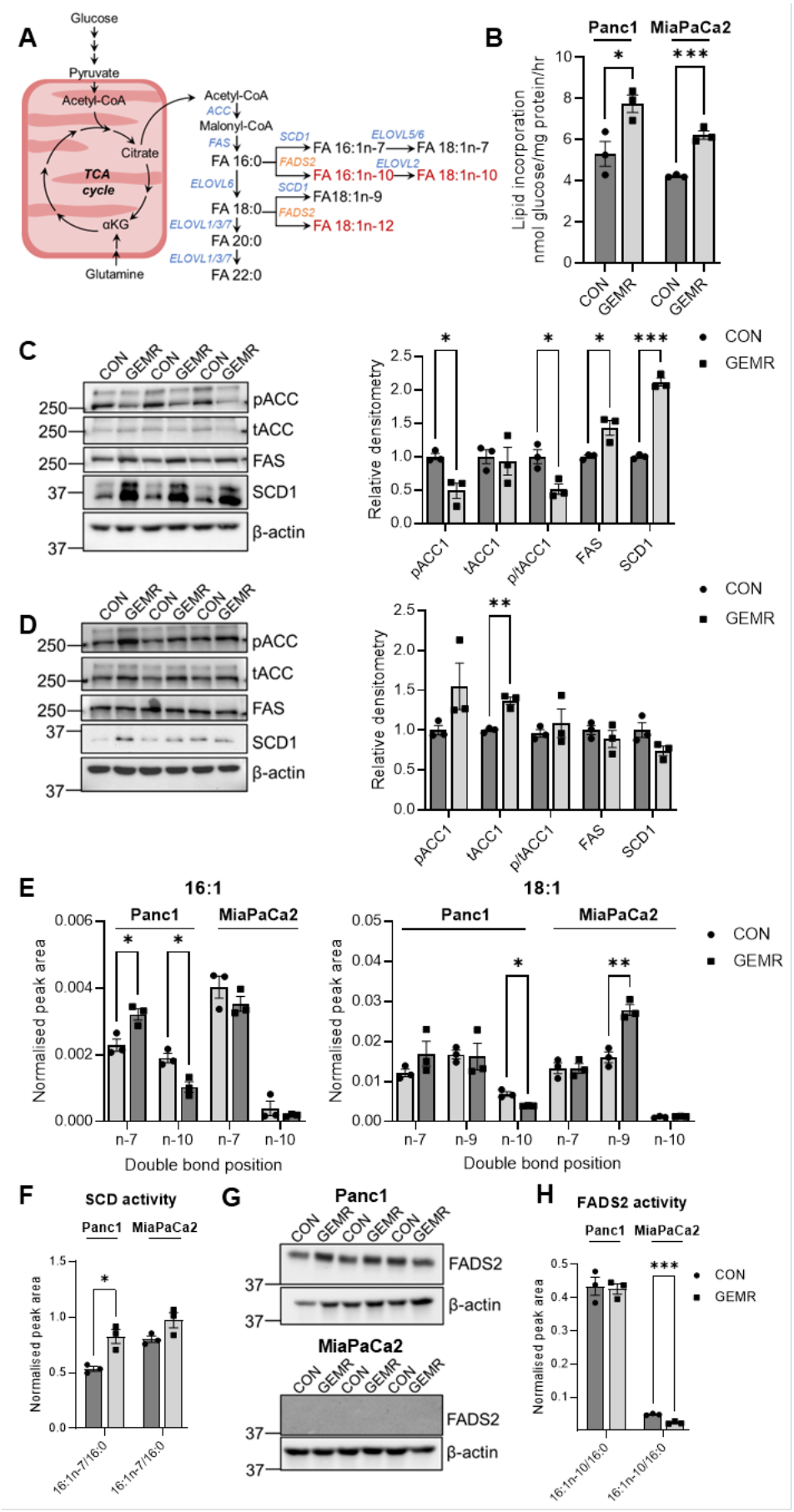
A
Glucose
Pyruvate
Acetyl-CoA
Citrate
TCA cycle
αKG
Glutamine
Acetyl-CoA
ACC
Malonyl-CoA
FAS
FA 16:0
ELOVL6
FA 18:0
ELOVL1/3/7
FA 20:0
ELOVL1/3/7
FA 22:0
SCD1
FA 16:1n-7
ELOVL5/6
FA 18:1n-7
FADS2
FA 16:1n-10
ELOVL2
FA 18:1n-10
SCD1
FA18:1n-9
FADS2
FA 18:1n-12
B
Panc1
MiaPaCa2
Lipid incorporation
nmol glucose/mg protein/hr
CON
GEMR
C
CON
GEMR
pACC
tACC
FAS
SCD1
β-actin
Relative densitometry
pACC1
tACC1
p/tACC1
FAS
SCD1
D
E
16:1
18:1
Normalised peak area
Double bond position
n-7
n-9
n-10
F
SCD activity
16:1n-7/16:0
G
FADS2
H
FADS2 activity
16:1n-10/16:0

163

164 **Figure 2: A** map of lipid synthesis in mammalian cells, including elongation and desaturation steps.
165 Canonical lipid synthesis pathways are shown in blue/black, while the alternative fatty acid desaturase
166 2 (FADS2)-mediated pathway is shown in red/orange. **B** *De novo* lipogenesis measured by tracing
167 uniformly radiolabelled glucose into the lipid fraction of control (CON) and gemcitabine resistant
168 (GEMR) Panc1 and MiaPaCa2 cells. Immunoblotting of key enzymes involved in *de novo* lipid
169 synthesis in **C** Panc1 and **D** MiaPaCa2 CON and GEMR cell lines. **E** Analysis of AMP^+-derivatised
170 isomeric FA16:1 and FA 18:1 MUFA by ozone-enabled fatty acid discovery (OzFAD). **F** SCD1 activity
171 measured by tracing uniformly labelled ^{13}C-palmitate (FA 16:0) into palmitoleic acid (FA 16:1*n*-7)
172 using liquid chromatography-mass spectrometry (LC-MS). **G** immunoblotting of FADS2. **H** FADS2
173 activity measured by tracing uniformly labelled ^{13}C-palmitic acid into sapienic acid (FA 16:1*n*-10) by
174 LC-MS. Unpaired t test, * $P < 0.05$, ** $P < 0.01$, *** $P < 0.001$. *ELOVL* elongation of very long chain
175 fatty acids *FADS2* fatty acid desaturase *FAS* fatty acid synthase 2 *pACC* phosphorylated acetyl-CoA
176 carboxylase *SCD1* stearoyl-CoA desaturase 1 *tACC* total ACC.

177 **GEMR increases stearoyl-CoA desaturase 1 (SCD1)-driven desaturation in Panc1 cells**

178 SCD1 is a Δ9-desaturase that inserts a carbon-carbon double bond at the 9th carbon from the carboxylate
179 end of either palmitic (16:0) or stearic (18:0) acid to form palmitoleic (FA 16:1*n*-7, *cis*) or oleic acid
180 (FA 18:1*n*-9, *cis*) respectively (where the *n-x* refers to the location of the carbon-carbon double bond
181 from the methyl end). Immunoblotting revealed increased abundance of SCD1 in Panc1 GEMR cells
182 (Figure 2C). This increase in SCD1 protein abundance could explain increased levels of MUFA-
183 containing lipids in Panc1 GEMR cells; however, recent work has demonstrated the presence of
184 FADS2-derived isomeric MUFA in other cancer types [35,36] that contain carbon-carbon double bonds at
185 locations distinct from SCD1-derived MUFA (Figure 2A, red/orange labels). Such isomers cannot be
186 differentiated using the LC-MS/MS method used for untargeted lipidomics analysis in Figure 1A&B.
187 To measure SCD1-derived fatty acids specifically in our GEMR PDAC cell lines we performed ozone-
188 enabled fatty acid discovery (OzFAD) [37] on AMP^+-derivatised MUFA (Figure 2E). These data showed
189 a statistically significant increase in SCD1-derived FA 16:1*n*-7 in Panc1 GEMR whereas SCD1-derived
190 FA 18:1*n*-9 was increased in MiaPaCa2 GEMR cells. To confirm these findings, SCD1 activity was
191 measured in both cell lines by measuring desaturation of uniformly labelled $^{13}C_{16}$ palmitate into $^{13}C_{16}$-
192 FA 16:1*n*-7 after 72 h. Baseline levels of FA 16:0 were not different between CON and GEMR cells of
193 either cell line (Figure S4A&B). Despite no change in labelled palmitate uptake in Panc1 cells (Figure
194 S4C), increased FA 16:1*n*-7/FA 16:0 was detected in GEMR Panc1 cells indicating enhanced SCD1
195 activity (Figure 2F). In contrast, no difference was observed in SCD1 activity for GEMR MiaPaCa2
196 cells despite a slight increase in labelled palmitate uptake (Figure S4D). Taken together, these data
197 suggest that GEMR upregulates SCD1 abundance and activity specifically in Panc1 cells.

198 **FADS2-derived monosaturated fatty acids are present in Panc1 cells**

199 Using OzFAD we were also able to detect the presence of Δ6 FADS2-derived *n*-10 isomers of FA 16:1
200 and FA 18:1 (*c.f.* Figure 2A) in both cell lines, with a greater amount of *n*-10 fatty acids found in Panc1
201 cells relative to MiaPaCa2 (Figure 2E). Both *n*-10 fatty acid isomers were lower in Panc1 GEMR cells
202 when compared with CON, with no changes detected in MiaPaCa2 GEMR cells. Immunoblotting for

203 FADS2 revealed no difference in abundance between Panc1 CON and GEMR cells; however, FADS2
204 protein was virtually undetectable in MiaPaCa2 cells (Figure 2G). Only trace amounts of *n*-12 isomers
205 (i.e. 18:0 FADS2-derived MUFA, *c.f.* Figure 2A) were detected in the Panc1 cell lines (data not shown),
206 suggesting a specific upregulation of Δ6 desaturation of FA 16:0 by FADS2. To further elucidate the
207 effect of GEMR on FADS2 we measured its steady-state activity by tracing uniformly labelled ^{13}C
208 palmitate into 16:1*n*-10 in both cell lines. No change in FADS2 activity was observed between CON
209 and GEMR Panc1 cells and a small but statistically significant decrease in FADS2 activity was seen in
210 MiaPaCa2 GEMR cells (Figure 2H). Overall, these data suggest that there is no specific increase in
211 FADS2 abundance or *n*-10 MUFA synthesis activity with GEMR in either cell line.

212 SCD1 and FADS2 compensate for each other when the alternate is knocked down in 213 Panc1 cells

214 To investigate if targeting lipid synthesis can improve the response of PDAC cells to GEMC treatment
215 we performed knockdown of key enzymes using small interfering RNA (siRNA). We targeted the genes
216 of key enzymes in lipid synthesis pathways including *ACACA* (*i.e.*, the gene encoding ACC1), *FASN*
217 (FAS), *SCD* (SCD1), and *FADS2*. We tested single siRNA targets against *ACACA* and *FASN* and
218 confirmed knockdown in Panc1 & MiaPaCa2 cells (Figure 3A). Knockdown of either *ACACA* or *FASN*
219 also resulted in large decreases in *de novo* lipogenesis as measured by tracing radiolabelled glucose into
220 the lipid fraction of CON Panc1 & MiaPaCa2 cell lines (Figure 3B). Two different siRNA targets were
221 tested for *SCD* and *FADS2*, with either showing good efficacy in the knockdown of their target (Figure
222 3C). Therefore, both siRNAs for *SCD* and *FADS2* were used in combination throughout.

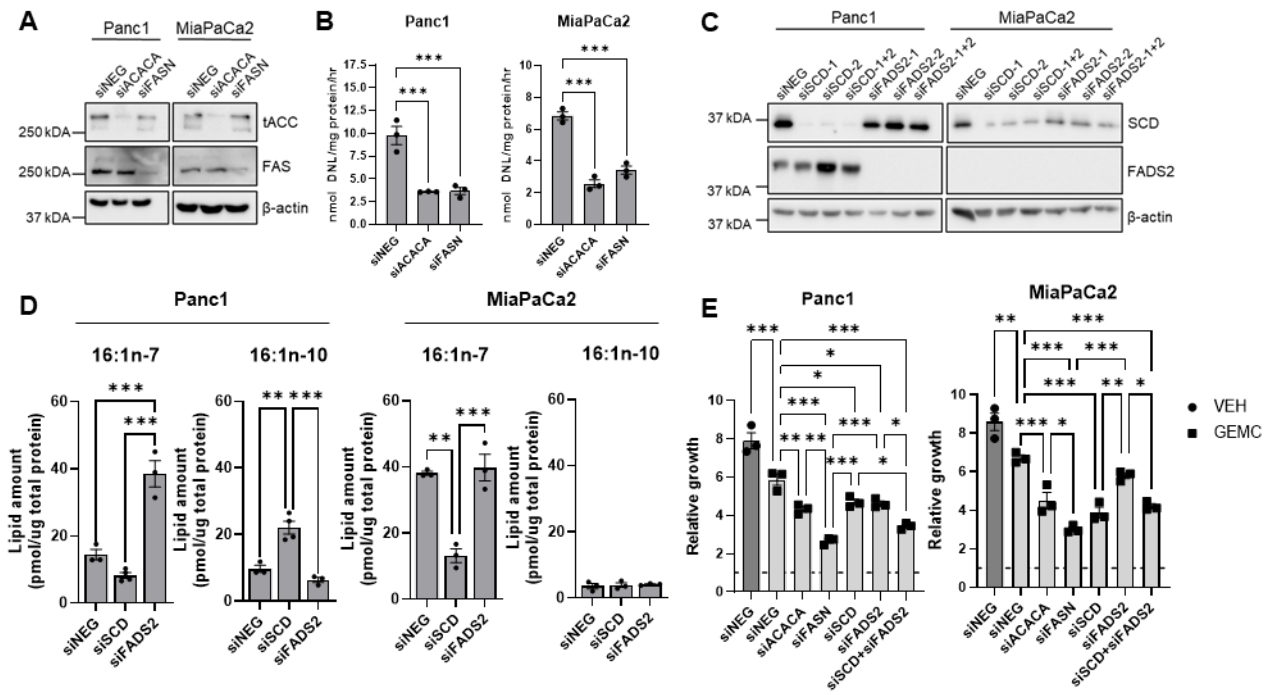

Figure 3: **A** Immunoblotting for ACC & FAS and **B** measurement of radiolabelled glucose into lipid fraction following knockdown of *ACACA* or *FASN*. **C** Immunoblotting for SCD1 & FADS2 or **D** quantification of 16:1 isomers measured by liquid chromatography-mass spectrometry following knockdown of *SCD* or *FADS2*. All measurements were performed following 72 h of siRNA transfection. **E** effect of 48 h GEMC treatment (Panc1 1 µM, MiaPaCa2 100 nM, or vehicle, VEH) on relative cell growth following 72 h knockdown of lipid synthesis enzymes. Cell growth was measured by crystal violet assay and normalised to start of siRNA knockdown (dashed line). Statistical significance was determined by **B** unpaired t test, or **D**&**E** one-way ANOVA with Tukey posthoc correction, *$P < 0.05$ ** $P < 0.01$. *** $P < 0.001$

We next measured the impact of SCD1 and FADS2 knockdown on the amount of 16:1 isomers by LC-MS/MS. In MiaPaCa2 cells, SCD1 knockdown had the intended effect where it significantly decreased FA 16:1*n*-7 levels (Figure 3D). Knockdown of FADS2 in MiaPaCa2 cells did not affect the amount of FA 16:1*n*-10; however, levels of FA 16:1*n*-10 (Figure 2E) and the abundance of FADS2 protein (Figure 2G&3C) are very low in this cell line. In contrast, knockdown of either desaturase in Panc1 cells did not decrease the expected isomeric MUFA product; instead, the alternate desaturation product increased in abundance (Figure 3D). For example, SCD1 knockdown in Panc1 cells resulted in a large increase in FA 16:1*n*-10, and while the amount of FA 16:1*n*-7 content did decrease relative to si*NEG* with SCD1 knockdown this reduction was not statistically significant. Likewise, the knockdown of FADS2 resulted in a large increase in FA 16:1*n*-7. Together these data suggest that each desaturase can compensate when the alternate is inhibited in Panc1 cells.

Knockdown of lipogenic enzymes improves GEMC efficacy in PDAC cells

Post validation of knockdown targets, we assessed if reducing the activity of the different lipid enzymes could improve GEMC chemotherapy efficacy on cell growth in Panc1 & MiaPaCa2 cells (Figure 3E).

247 Target enzymes were knocked down in Panc1 & MiaPaCa2 cells for 72 h prior to 48 h of treatment
248 with vehicle (VEH) or a dose of GEMC tailored to induce a statistically significant decrease in si*NEG*
249 cell growth (Panc1 1 μM, MiaPaCa2 100 nM). Knockdown of *ACACA*, *FASN*, *SCD* or *FADS2*
250 combined with GEMC treatment resulted in decreased cell growth in Panc1 cells when compared with
251 GEMC-treated si*NEG* controls, with si*FASN* producing the greatest effect (Figure 3E). *ACC, SCD* or
252 *FADS2* knockdown each had an equivalent impact on cell growth. However, co-targeting desaturases
253 using si*SCD* and si*FADS2* produced a significantly greater decrease in Panc1 cell growth than targeting
254 either enzyme alone, with the effect of dual desaturase knockdown on cell growth being comparable to
255 that of si*FASN* (Figure 3E). All reported decreases in cell growth following concomitant knockdown
256 and GEMC treatment were above that for knockdown alone for all targeted genes except *FASN*, which
257 had a similar impact on growth with or without GEMC treatment (Figure S5A). Knockdown of key
258 lipid synthesis enzymes in combination with GEMC treatment in MiaPaCa2 cells showed a similar
259 trend to that of Panc1, except that si*FASN* or si*SCD* produced a comparable decrease in relative cell
260 growth a (Figure 3E). Knockdown of *FADS2* did not significantly decrease cell growth in MiaPaCa2
261 cells, and, not surprisingly, co-targeting both desaturases with si*SCD* and si*FADS2* in MiaPaCa2 cells
262 produced no additional effect when compared with si*SCD* (Figure 3E). The effect of combined
263 knockdown with GEMC treatment was above that of knockdown only for *ACACA* and *FADS2* in
264 MiaPaCa2 cells (Figure S5B). We also measured the effect of knockdown of lipid synthesis enzymes
265 in GEMR cells; however, only si*FASN* resulted in decreased cell growth on either cell line (Figure
266 S5C&D). Collectively, these data suggest that targeting key enzymes involved in fatty acid synthesis
267 can successfully sensitise GEMC-naïve PDAC cells to GEMC treatment, and that where alternate
268 desaturase activity exists co-targeting both desaturases is necessary to have the greatest impact on cell
269 growth.

270 **Combination GEMC/paclitaxel resistance also upregulates lipid synthesis**

271 GEMC monotherapy has long been the first-line treatment for metastatic PDAC, but is now more
272 typically given in combination with nab-paclitaxel [38]. To test the effect of combination chemotherapy
273 on *de novo* lipogenesis in PDAC we attenuated Panc1 and MiaPaCa2 cells to grow in GEMC/paclitaxel
274 (PTX) by a similar regime to that of GEMR induction using a ratio of 10:1 (GEMC:PTX) to
275 approximate the typical ratio given to PDAC patients [39,40]. In Panc1 cells the final concentration was 28
276 nM GEMC (2.8 nM PTX), and 8 nM GEMC (0.8 nM PTX) for MiaPaCa2 cells. Combination therapy
277 attenuated (CombAT) Panc1 and MiaPaCa2 cells showed improved growth and proliferation in media
278 containing 15 nM GEMC/1.5 nM PTX when compared to naïve control cells, suggesting that resistance
279 was present in both cell lines (Figure S6). We next performed untargeted lipidomics to determine
280 relative changes in lipid species across both cell lines (Figure 4A&B). These data revealed extensive
281 increases across 166 lipid species in Panc1 CombAT cell lines compared with CON, including increases
282 in many triacylglycerol (TG) species and total TG (Figure 4A). Increases were also seen in several TG

283 species in CombAT MiaPaCa2 cells, with 30 lipid species increased in total when compared with CON
284 (Figure 4B). Together these data suggest that the addition of PTX to GEMC chronic treatment does not
285 abrogate the lipogenic phenotype observed with monotherapy GEMR, and, in fact, may enhance *de*
286 *novo* lipogenesis in both cell lines.

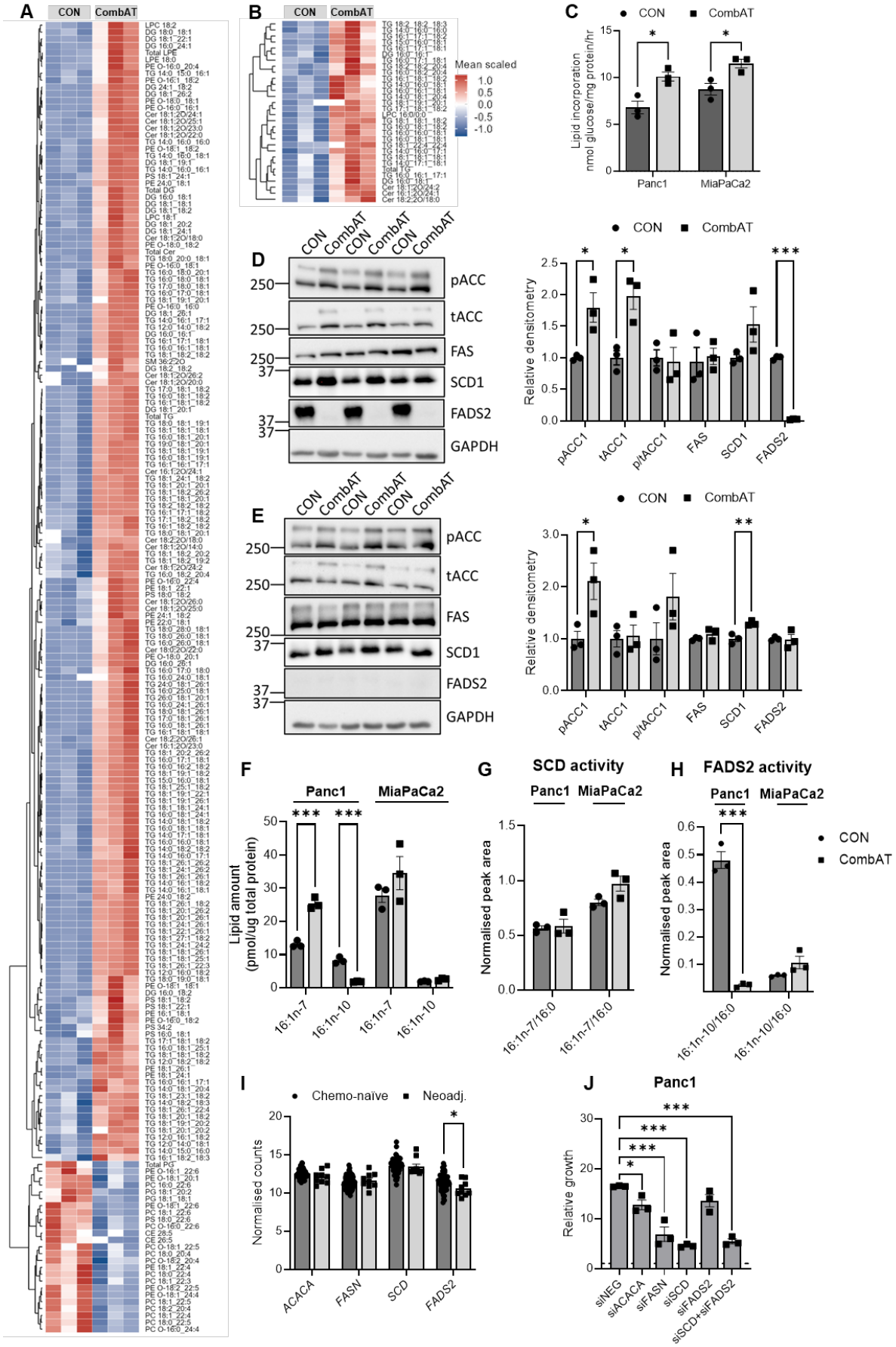
A
CON
CombAT
B
CON
CombAT
Mean scaled
1.0
0.5
0.0
-0.5
-1.0
C
CON
CombAT
Lipid incorporation nmol glucose/mg protein/hr
Panc1
MiaPaCa2
D
CON
CombAT
pACC
tACC
FAS
SCD1
FADS2
GAPDH
Relative densitometry
pACC1
tACC1
p/tACC1
E
F
Panc1
MiaPaCa2
Lipid amount (pmol/ug total protein)
16:1n-7
16:1n-10
G
SCD activity
Normalised peak area
16:1n-7/16:0
H
FADS2 activity
16:1n-10/16:0
I
Chemo-naïve
Neoadj.
Normalised counts
ACACA
FASN
SCD
FADS2
J
Panc1
Relative growth
siNEG
siACACA
siFASN
siSCD
siFADS2
siSCD+siFADS2

287

288 **Figure 4:** Untargeted lipidomics of both **A** Panc1 and **B** MiaPaCa2 control (CON) and combination
289 therapy attenuated (CombAT) cell lines (unpaired t-test, $P < 0.01$). **C** *De novo* lipogenesis measured by
290 the incorporation of radiolabelled glucose into the lipid fraction. Immunoblotting for total and activated
291 key lipid synthesis enzymes in **D** Panc1 and **E** MiaPaC2 CON and CombAT cells. **F** 16:1 fatty acid
292 isomers measured by LC-MS of AMP^+-derivatised fatty acids. Measurement of **G** SCD1 and **H** FADS2
293 activity in Panc1 and MiaPaCa2 CON and CombAT cell lines by tracing uniformly stable-labelled
294 palmitic acid into isomeric MUFA. **I** Analysis of PDAC tumour RNAseq data published by Zhou and
295 colleagues obtained from patients who underwent surgical resection prior to chemotherapy (chemo-
296 naïve) or received GEMC/nab-paclitaxel neoadjuvant treatment (Neoadj.) before tumour resection. **J**
297 Effect of 72 h knockdown of lipid synthesis enzymes on Panc1 CombAT cell growth. Statistical
298 significance was determined by unpaired t test (**A-I**) or one-way ANOVA with Tukey posthoc
299 comparisons with *si*NEG only (**J**). *$P < 0.05$ ** $P < 0.01$. *** $P < 0.001$.

300 We next assessed if increased *de novo* lipogenesis persisted in our CombAT cell lines, with both Panc1
301 and MiaPaCa2 CombAT cells demonstrating increased radiolabelled glucose incorporation into the
302 lipid fraction (Figure 4C). Immunoblotting for key lipogenic enzymes showed increases in total and
303 phosphorylated ACC1 in Panc1 CombAT cells (Figure 4D), alongside increased levels of
304 phosphorylated ACC1 in MiaPaCa2 combat cells (Figure 4E). A small but statistically significant
305 increase in SCD1 abundance was also detected in MiaPaCa2 CombAT cells.

306 Combination chemotherapy resistance decreases FADS2 abundance and activity in 307 Panc1 cells

308 Surprisingly, FADS2 protein abundance was substantially decreased in Panc1 CombAT cells (Figure
309 4D). Similar to GEMR cell lines, little to no FADS2 protein was detected in MiaPaCa2 CombAT or
310 CON cells (Figure 4E). To confirm decreased FADS2 abundance in Panc1 CombAT cells we measured
311 FA 16:1 isomers in both cell lines by LC-MS/MS and found increased FA 16:1*n*-7 in Panc1 CombAT
312 cells alongside substantially decreased FA 16:1*n*-10 (Figure 4F). Also observed in Panc1 CombAT
313 were changes in PUFA profile consistent with FADS2 downregulation, including decreases in FA
314 22:6*n*-3, FA 18:3*n*-6, FA 20:4*n*-6, FA 22:4*n*-6 and FA 22:5*n*-6 when compared with CON (Figure S7).
315 No changes were detected in FA 16:1 isomeric profile in MiaPaCa2 CombAT cells when compared to
316 CON (Figure 5F), alongside no changes in PUFA levels (Figure S7C). To further confirm these
317 findings, we measured steady-state desaturase activity by tracing uniformly labelled ^{13}C-palmitate into
318 both cell lines over 72 h. Neither cell line exhibited any differences between CON and CombAT cells
319 in unlabelled FA 16:0 content (Figure S8A&B). However, Panc1 CombAT cells had more labelled
320 palmitic acid (relative to unlabelled palmitic acid) while MiaPaCa2 CombAT cells had less (Figure
321 S8C&D respectively). No differences were seen for SCD1 activity as measured by the ratio of labelled
322 FA16:1*n*-7 to FA 16:0 in Panc1 or MiaPaCa2 CombAT cells (Figure 4G). A substantial decrease in FA
323 16:1*n*-10/16:0 was detected in Panc1 CombAT cells, indicating a reduction in FADS2 activity, with no
324 change in FA 16:1*n*-10/FA 16:0 observed for MiaPaca2 CombAT cells (Figure 4H). Also apparent in
325 Panc1 CombAT cells was a marked decrease in FAO compared with CON cells (Figure S9). Taken
326 together, these data indicate that chronic combination GEMC/PTX treatment strongly downregulates

327 FADS2 abundance and activity in the Panc1 cell line. To explore if combination GEMC/PTX therapy
328 might exhibit the same effect on lipid metabolism in human PDAC patients, we analysed recently
329 published RNA-seq data obtained from PDAC patients who received no treatment (chemo-naïve) or
330 GEMC/nab-paclitaxel neoadjuvant chemotherapy prior to tumour resection [41]. The data showed no
331 difference in the expression of *ACACA, FASN or SCD* between chemo-naïve or neoadjuvant-treated
332 tumours; however, the neoadjuvant group demonstrated a small but statistically significant decrease in
333 *FADS2* expression when compared with chemo-naïve tumours (Figure 4I).

334 Given the effect of combination therapy resistance on FADS2 abundance and fatty acid isomer profile
335 we sought to understand if co-targeting both desaturases was still necessary to decrease in cell growth
336 in Panc1 CombAT cell lines. Knockdown of *ACACA*, *FASN*, or *SCD* for 72 h in Panc1 CombAT cells
337 resulted in a statistically significant decrease in cell growth when compared to negative siRNA control
338 (si*NEG*), with si*FASN* or si*SCD* producing the largest decreases in cell growth (Figure 5J). Panc1
339 CombAT cells were insensitive to *si*FADS2 knockdown, and no additional effect on cell growth was
340 observed with co-knockdown of SCD. These data suggest that therapeutically targeting SCD1 in
341 combination with GEMC/PTX chemotherapy could be a viable strategy for enhancing cytotoxicity in
342 PDAC.

343 Discussion

344 We sought to characterise metabolic adaptations to chemotherapy exposure in PDAC and found
345 enhanced *de novo* lipogenesis in PDAC cells with resistance to both monotherapy GEMC and
346 combination GEMC/PTX chemotherapy. Enhanced *de novo* lipogenesis is a known feature of many
347 cancers, including pancreatic cancer [18], where increased expression of lipogenic genes is correlated with
348 poorer survival and greater resistance to chemotherapy [17]. Herein we provide the first report of enhanced
349 *de novo* lipogenesis specifically in GEMC resistance in PDAC, providing a novel target for the disease
350 that could potentially improve treatment efficacy. We also provide the first report of FADS2-derived *n*-
351 10 MUFA in PDAC (Figure 2E). The ability of cancer cells to exhibit diversity in isomeric lipids has
352 recently been described in other cancer cell types including liver & lung cancer cell lines more
353 extensively in prostate cancer [35,36]. This metabolic and isomeric diversity is proposed to promote
354 metabolic plasticity enabling cancer cells to survive and proliferate in challenging tumour
355 microenvironments depleted in bioenergetic fuels and oxygen.

356 In this work we specifically found upregulation of ACC1 (through increased total abundance or
357 decreased phosphorylation at Serine-79), FAS and SCD with GEMR. FAS is commonly expressed at
358 high levels in a variety of cancers of human tissues [23–25] and *FASN* overexpression correlates to poorer
359 survival and increased GEMC resistance in PDAC [17]. High FAS levels have also been found in the
360 serum of patients with PDAC or intraductal papillary mucinous neoplasms [42]. We found that genetically
361 inhibiting FAS (Panc1 & MiaPaCa2), SCD1 (MiaPaCa2) or SCD1 & FADS2 (Panc1) in combination

362 with GEMC produced the greatest impact on PDAC cell growth (Figure 4E). Previous work
363 demonstrated that inhibition of FAS by Orlistat induces ER stress and acts synergistically with GEMC
364 to decrease PDAC cell growth and reduce tumour burden in xenograft models of PDAC [17]. Orlistat has
365 also been reported to attenuate oxaliplatin resistance in colorectal cancer [43]. This synergistic effect of
366 Orlistat with chemotherapy *in vivo* may be related to a direct effect on FAS but may also arise from the
367 dual action of Orlistat on lipases that further inhibit the availability of free fatty acids for use by cancer
368 cells. However, Orlistat has poor bioavailability, is contraindicated in pancreatic disease, and can cause
369 pancreatitis in susceptible patients [44], all of which potentially limit its therapeutic use in PDAC. Other
370 small molecule inhibitors of FAS have had some success in decreasing cancer cell growth, including in
371 breast, colon, lung, colorectal, bladder, ovarian, gastric, endometrial, prostate, and gastrointestinal
372 cancers as well as in melanoma and lymphoma (reviewed extensively by [23]). Cerulenin has previously
373 been shown to re-sensitise cisplatin-resistant ovarian cancer cell lines to treatment [45], while its more
374 stable derivative C75 sensitises breast cancer cells to cisplatin treatment [46]. However, both cerulenin
375 and C75 exhibit significant off-target and side effects that preclude their clinical use [23]. Newer FAS
376 inhibitors TVB-3166 and fasnall show promise for synergistically inhibiting cell viability when
377 combined with tubulin-stabilising drugs in taxane-resistant prostate cancer [47]. Mouse and human-
378 derived mutant $KRAS^{G12D}$ lung cancer models are sensitive to genetic or TVB-3664 inhibition of FAS
379 [48]. Moreover, high *FASN* and *SCD* expression are correlated with mutant $KRAS^{G12D}$ in lung cancer [48],
380 which could potentially explain the differences between the two PDAC cell lines examined herein –
381 Panc1 cells similarly contain $KRAS^{G12D}$ and GEMR increased expression and activity of both lipogenic
382 enzymes, while MiaPaCa2 cells contain $KRAS^{G12C}$ (Table S1). In any event, targeting FAS could
383 provide therapeutic benefits to PDAC patients when combined with GEMC-based therapy; however, a
384 small molecule inhibitor with good efficacy and a low side effect profile would need to be developed.

385 SCD1 has been described as an oncogene in lung cancer [49] and explored as a potential therapeutic target
386 for several cancers including PDAC (reviewed by [50]). SCD1 is highly expressed in the exocrine pancreas
387 [51] and increased expression of SCD1 in cancer-associated fibroblasts correlates with decreased PDAC
388 survival time and GEMC resistance [16]. Higher levels of FA 16:1 and 18:1 are associated with aggressive
389 subtypes of PDAC immortalised cells; however, positions of unsaturation (*i.e.*, fatty acid isomers) were
390 not determined in this work [31]. Inhibition of SCD1 using the small molecule inhibitor A939572 induces
391 the unfolded protein response and decreases the growth of pancreatic tumours in KPC mice and in
392 $EPCAM^{+}$ organoids derived from KPC mouse tumours [52]. In this work, we also discovered significant
393 FADS2-derived *n*-10 MUFA desaturase products in the Panc1 cell line (Figure 2E). There is limited
394 exploration of FADS2 as a therapeutic target in cancer and existing data has largely focused on its role
395 in Δ6 desaturation of PUFA [53,54]. FADS2 inhibition by small molecule inhibitor sc-26196 suppresses
396 prostaglandin E2 production via arachidonic acid and sensitises glioblastoma cells to radiotherapy in a
397 xenograft model [55]. Genetic or pharmacological FADS2 inhibition also suppresses colon, lung,

398 melanoma, and cholangiocarcinoma cancer cell tumour growth in xenograft and genetically engineered
399 models [56–58]. Pharmacologic or genetic dual-inhibition of SCD1 and FADS2 decreases tumour and
400 metastatic lesion growth and cancer stem cell formation in ovarian cancer while reducing resistance to
401 platinum-based chemotherapy [54]. Our work and others [35,36] observed overcompensation by the
402 alternative desaturation pathway when SCD1 or FADS2 are individually inhibited in cancer cells
403 (Figure 4D). Indeed, this same compensatory desaturase effect might explain the observed decrease in
404 16:1*n*-10 and 18:1*n*-10 in Panc1 GEMR cells, where SCD1 abundance, activity, and MUFA products
405 were all increased when compared with Panc1 CON cells (Figure 2C, E, &F). Similarly, an increase in
406 *FADS2* expression has been observed when cell lines resistant to SCD1-inhibitors (A549 & HeLa) are
407 treated with A939572 [59]. We show suboptimal inhibition of PDAC cell growth when only one
408 desaturase is silenced alongside co-treatment with GEMC (Figure 4E). Therefore, the use of SCD1
409 inhibitors might be suboptimal in the presence of significant FADS2 abundance or activity; however,
410 the extent of FADS2 protein abundance or activity in PDAC tumours on a population level is not yet
411 fully known.

412 This phenomenon of competing inhibitory pathways has previously been described and is thought to
413 enable enhanced plasticity at the expense of maximised proliferation [36,60,61]. Such competing pathways
414 might also promote cancer cell survival in PDAC as the hypoxic, nutrient-depleted tumour
415 microenvironment is particularly enhanced by the dense fibrosis associated with the disease [62].
416 Desaturation is a highly energy-demanding process, and desaturases are NADPH, O_2, and cytochrome
417 b5 dependent [63] - all of which are likely in short supply in the tumour microenvironment. Specifically
418 in PDAC, mutant *KRAS* regulates GOT1 synthesis of NADPH from glutamine to maintain redox status
419 [64], but feasibly this pathway could also support high NADPH levels to maintain enhanced lipid synthesis
420 and desaturation. Though highly energy-demanding, desaturation would allow the sequestration of
421 highly lipotoxic SFA such as FA 16:0 and FA 18:0 into less toxic MUFA in lipogenic cells, thus
422 preventing cell death [65]. Increased desaturation of lipids also modulates cell membrane fluidity and is
423 highly associated with epithelial-to-mesenchymal transition (EMT). This process is crucial for cell
424 migration and metastatic initiation [66,67], and FADS2-derived FA 16:1*n*-10 specifically promotes cell
425 migration in melanoma cells [68]. Expression of EMT transcription factor Zeb1 has been shown to
426 promote increased PUFA to MUFA ratio within cancer cells, with downregulation of Zeb1 suppressing
427 FADS2 and enhancing SCD1 & FAS expression [69]. MUFA are also less susceptible to peroxidation by
428 reactive oxygen species (ROS) than PUFA, and given that ROS levels are often high in PDAC and other
429 cancers [70,71] increased MUFA would limit both ROS and cell death from iron-driven lipid peroxidation
430 (*i.e.* ferroptosis). Indeed, cells cultured with exogenous sources of MUFA have suppressed ferroptosis
431 [72] and SCD1 overexpression protects ovarian cancer cells from ferroptosis-mediated cell death [73].
432 Similarly, pharmacological inhibition of SCD1 sensitises cancer cells expressing high levels of Zeb1 to

433 ferroptosis [69]. In short, despite the high energy demands associated with lipid desaturation the process
434 likely provides significant benefits for cancer cell survival that outweigh the energetic cost.

435 Our finding that combination GEMC/PTX resistance strongly and very specifically downregulates
436 FADS2 protein abundance and activity in Panc1 cells was unexpected. Single-dose combination
437 GEMC/nab-paclitaxel downregulates *de novo* lipogenesis in PDAC cells via the AMP-activated protein
438 kinase/ sterol regulatory element-binding protein 1 (SREBP1) axis [74]. However, PTX treatment has also
439 previously been shown to increase FADS2 protein abundance in lung adenocarcinoma cells [75]. The
440 mechanism by which PTX combined with GEMC specifically downregulates FADS2 protein levels and
441 activity is unknown, and FADS2 shares similar transcriptional factors to ACC, FAS and SCD1 [76].
442 Upregulated *FADS2* expression and increased sapienic acid biosynthesis can be driven in multiple
443 cancer cell lines through increased mammalian target of rapamycin (mTOR) signalling and SREBP [77];
444 however, little else is known about transcriptional or post-translational regulation of FADS2 abundance
445 and activity. Nevertheless, our results strongly suggest that combining SCD1 inhibition with
446 GEMC/PTX chemotherapy could be an effective broad-spectrum strategy for decreasing PDAC cell
447 growth that could benefit patients both with or lacking significant dual desaturase activity. This could
448 be important for accelerated translational efforts as a therapeutic target as only a single small molecule
449 inhibitor is currently available for FADS2 (sc-26196), and its *in vivo* safety and efficacy profile is yet
450 to be established in humans. Importantly PDAC patients who received GEMC/PTX neoadjuvant
451 treatment show decreased *FADS2* expression (Figure 5I), further highlighting the potential
452 translatability of our findings.

453 In summary, we have identified that *de novo* lipogenesis is increased in GEMC-resistant PDAC cells
454 including the presence of an alternate desaturation pathway in Panc1 cells. We identify several key lipid
455 metabolic pathways including ACC1, FAS, SCD1 and FADS2 that could be targeted to improve GEMC
456 efficacy on cell growth. Importantly, we have determined that SCD1 and FADS2 can compensate for
457 each other in PDAC, and that where dual desaturase activity exists both desaturases must be targeted to
458 provide the best effect. Finally, we provide evidence that combination GEMC/PTX therapy strongly
459 and specifically downregulates FADS2 expression and activity and increases the efficacy of SCD1
460 inhibition in PDAC cells with dual desaturase activity. Therefore, we conclude that co-targeting lipid
461 synthesis in PDAC could be a viable strategy for improving the efficacy of both GEMC monotherapy
462 and combination GEMC/PTX therapy in patients.

463 # Materials and method

464 ## Materials

465 Gemcitabine hydrochloride, paclitaxel and foetal calf serum (FCS) were purchased from BioStrategy
466 (Melbourne, VIC, Australia). High glucose Dulbecco's Modified Eagle's medium (DMEM) was
467 purchased from ThermoFisher Scientific (Melbourne, VIC, Australia). All solvents and additives used
468 for liquid chromatography-mass spectrometry (LC-MS) were HPLC grade or higher and were
469 purchased from ThermoFisher Scientific. Crystal violet and LC-MS grade water were purchased from
470 Merck Life Sciences (Melbourne, VIC, Australia). All lipid internal standards were purchased from
471 Merck Life Sciences except diacylglycerol 15:0/15:0 (Nu-Chek Prep, Elysian, MN, USA) and d5-
472 triacylglycerol 16:0/16:0/16:0 (C/D/N Isotopes, Quebec, Canada). Antibodies for immunoblotting were
473 purchased from Cell Signaling Technology (Danvers, MA, USA), Abclonal (Woburn, MA, USA)
474 Abcam (Melbourne, VIC, Australia), or Santa Cruz Biotechnology (Dallas, TX, USA) as indicated in
475 Table S1. MUFA isomer standards were purchased from Sapphire Bioscience (Sydney, NSW,
476 Australia).

477 ## Cell culture & chemotherapy resistance generation

478 Panc1 and MiaPaCa2 cells from ATCC were cultured in high glucose DMEM containing 4.5 g/L
479 glucose and were supplemented with 10% FCS. Cells were cultured under 5% CO_2 at 37ºC and routinely
480 passaged every 2-3 days (when ~80-90% confluent). GEMC resistance was induced in PDAC cell lines
481 through increasing doses over 10-12 weeks. Each cell line was treated with the highest tolerable dose
482 of gemcitabine for 48 h and allowed to recover until normal proliferation was observed (1-3 weeks).
483 This process was repeated a minimum of three times before comparing the half-maximal inhibitory
484 concentration (IC_{50}) with untreated cells of the same PDAC line. If the IC_{50} in the GEMC-treated group
485 was higher than CON then resistance was determined to have been established. If not, then the
486 concentration of GEMC was increased, and the process repeated. CombAT cells were generated
487 similarly through repeat escalating doses of GEMC/PTX (10:1 v/v) for 12 weeks.

488 ## Measurement of half-maximal inhibitory concentration

489 The IC_{50} was determined using a crystal violet assay. Cells were seeded at 1×10^4 cells/well into a 96-
490 well plate in triplicate and allowed to adhere overnight. The next day cells were treated with serial
491 dilutions of GEMC (phosphate buffered saline, PBS, as vehicle) or GEMC:PTX (10:1, with PBS+0.1%
492 ethanol as the vehicle). The IC_{50} was measured after 48 h by crystal violet assay. Media was removed
493 from adherent cells and cells were washed once with PBS. Cells were fixed in a solution of 0.5% w/v
494 crystal violet in 50% v/v methanol for ≥10 min. After fixation, cells were washed with water to remove
495 excess crystal violet and allowed to dry overnight. Stained adherent cells were then solubilised in 1%
496 w/v SDS by vigorous shaking for several hours and the absorbance was read at 570 nm. Absorbance

497 values were normalised to the vehicle and the IC_{50} was calculated by a non-linear regression by fitting
498 the log_{10} transformed drug concentration against relative cell viability. Statistical significance was
499 determined by comparing a four-parameter curve fit using the extra sum of squares F test ($P < 0.05$).

500 **BODIPY staining and confocal imaging**

501 For BODIPY staining and confocal imaging, cells were seeded in a 96 well plate at 10,000 cells/well
502 and allowed to grow to near-confluency. Cells were then fixed with 4% paraformaldehyde for 10 min
503 at room temperature, followed by PBS washes. Permeabilization was performed for 10 min using a
504 saponin-based permeabilization/blocking buffer (0.2% (w/v) saponin, 4% (v/v) FCS, 1% (w/v) bovine
505 serum albumin (BSA), and 0.02% (v/v) sodium azide in PBS). Next, cells were incubated for 2 h with
506 Alexa Fluor® 647 anti-Tubulin-α antibody (1:250 dilution, clone 10D8, BioLegend) prepared in the
507 permeabilization/blocking buffer. After several washes with PBS, 200 nM BODIPY 493/503 (Cat. No.
508 25892, Cayman Chemical) and Hoechst 33342 (10 µg/mL, B2261-25MG, Sigma-Aldrich) were added
509 in permeabilization buffer for 10 min at room temperature, followed by PBS washes. Confocal images
510 were acquired using an LSM900 confocal laser scanning microscope with a 40x objective. Lipid
511 droplets per cell and droplet size were quantified using Fiji software.

512 **Lipid extraction**

513 Lipids were extracted from cells grown to 80-90% confluency in 6 well plates using a modified methyl
514 *tert*-butyl ether (MTBE) method [78,79]. Adherent cells were washed with ice-cold PBS and scraped into
515 methanol containing 0.01% butylated hydroxytoluene and 100 pmol of internal standards
516 (phosphatidylcholine 19:0/19:0, phosphatidylethanolamine 17:0/17:0, phosphatidylserine 17:0/17:0,
517 lysophosphatidylcholine 17:0, lysophosphatidylethanolamine 14:0, phosphatidylglycerol 17:0/17:0,
518 phosphatidic acid 17:0/17:0, ceramide d18:1/17:0, dihydrosphingomyelin 12:0, cholesteryl ester 22:1,
519 diacylglycerol 17:0/17:0, D_5-triacylglycerol 16:0/16:0/16:0 and cardiolipin 14:0/14:0/14:0/14:0). An
520 empty well was also scraped for use in background subtraction. To this, MTBE was added at a ratio of
521 3:1 v/v, and extracts were rotated overnight at 4ºC. Following overnight rotation, 1 part of ice-cold 150
522 mM ammonium acetate was added, samples were vortexed vigorously and centrifuged at 2000 *x g* for
523 5 min. The upper organic phase containing lipids was transferred into a 1.5 mL autosampler vial and
524 dried under N_2 at 37ºC Dried lipids were reconstituted in chloroform:methanol:water (60:30:4.5 v/v/v),
525 transferred to a sleeved vial, and stored at -20ºC until analysis. The aqueous phase containing the protein
526 pellet was dried under N_2 and digested with 1M NaOH overnight at 4ºC. Digested protein was diluted
527 1:2 v/v with water and protein concentration was determined using a Pierce BCA assay kit
528 (ThermoFisher Scientific)

529 **Untargeted lipidomics**

530 Untargeted lipidomics was performed as previously described [80] using a Dionex Ultimate 3000 LC
531 pump and Q Exactive Plus mass spectrometer equipped with a heated electrospray ionization (HESI)
532 source (ThermoFisher Scientific, Waltham, MA, USA) [81–83]. Lipids were separated on a core-shell
533 hybrid C18 reverse-phase column (ACQUITY C18 CSH, 2.1 x 100 mm, 1.7µm pore size, Waters Corp.,
534 Milford, MA) using a binary gradient, where mobile phase A consisted of acetonitrile:water (6:4 v/v)
535 and B of isopropanol: acetonitrile (9:1 v/v). Both mobile phases A and B contained 10 mM ammonium
536 formate and 0.1% formic acid. The autosampler was kept chilled at 10ºC, the column was heated to
537 60ºC, and the flow rate was maintained at 0.26 ml/min. Source conditions were as follows: a spray
538 voltage 4.0 kV in positive ion mode and 3.5 kV in negative ion mode, capillary temperature 290°C, S
539 lens RF 50, and auxiliary gas heater temperature of 250°C. Nitrogen was used as both source and
540 collision gas, with the sheath gas flow rate set at 20 and the auxiliary gas flow rate at 5 (arbitrary units).
541 Data were acquired in full scan/data-dependent MS2 mode (full-scan resolution 70,000 FWHM, max
542 ion injection time 50 ms, scan range m/z 200–1,500), with the 10 most abundant ions being subjected
543 to collision-induced dissociation using an isolation window of 1.5 Da and a normalized stepped
544 collision energy of 15/27 eV. Product ions were detected at a resolution of 17,500. An exclusion list for
545 background ions was developed using extraction blanks, and mass calibration was performed in both
546 positive and negative ionization modes before analysis to ensure mass accuracy of 5 ppm in full-scan
547 mode.

548 Lipids were identified using MS-DIAL v4.9 [84]. Lipids were detected in both positive and negative
549 ionization modes using a minimum peak height of $1x10^4$ cps, an MS1 tolerance of 5 ppm and MS2
550 tolerance of 10 ppm, and a minimum identification score of 50%. Identified peaks were aligned with a
551 retention time (RT) tolerance of 0.5 min. Exported aligned data were background subtracted, quantified
552 from internal standards, and normalised to protein using the statistical package R.

553 ***De novo* lipogenesis assay using [U-14]C labelled glucose**

554 Cells were seeded in 6 well plates and allowed to grow to near-confluency (80-90%, ~$1\text{-}2\times10^6$
555 cells/well). Briefly, cells were washed with PBS and incubated in DMEM containing 1 g/L D-glucose
556 and 2 µCi/mL [U-14C]C-glucose (Perkin Elmer, Sydney, NSW, Australia) for 2 h at 37°C. Following
557 this, cells were washed and scraped into ice-cold PBS. Cells were lysed by passing repeated through a
558 fine gauge needle, and an aliquot was taken for protein determination by BCA assay. Lipids were
559 extracted from the remaining sample by Folch extraction [85]. The lower lipid-containing organic phase
560 was removed to a new vial and dried under N_2 at 37ºC before being reconstituted in scintillation fluid
561 (Ultima Gold, Perkin Elmer, Sydney, NSW, Australia). ^{14}C content was determined by direct DPM
562 assay using a beta counter (TriCarb liquid scintillation counter, Perkin Elmer) and normalised to total
563 protein.

564 **Western blotting**

565 For immunoblotting of lipid synthesis enzymes cells were grown to near-confluency on 6 well plates
566 (~1-2×10^6 cells/well). Cells were washed with ice-cold PBS and scraped into ice-cold
567 radioimmunoprecipitation assay buffer containing protease and phosphatase inhibitors (10 µg/mL
568 phenylmethylsulfonyl fluoride, 10 µg/mL aprotinin, 10 µg/mL leupeptin, 1 mM Na_3VO_4, and 10 mM
569 NaF). Cells were lysed by repeated freeze/thawing on ice using liquid N_2, before being centrifuged at
570 16,100 *x g* (4ºC) for 5 min. The supernatant was removed to a new vial, from which the protein
571 concentration was determined by BCA assay. Lysates were resuspended in laemelli buffer, and 10-15
572 ug of protein was separated by SDS polyacrylamide gel electrophoresis (10%). Proteins were
573 transferred onto 0.2 µm polyvinylidene fluoride membrane and protein bands visualised by Ponceau S
574 staining. Destained membranes were blocked in 5% w/v skim milk in Tris-buffered saline containing
575 0.1% Tween20 (TBST) for 1 h, before being incubated in primary antibody (1:1000) overnight (Table
576 S2). Membranes were washed with TBST before being incubated with an appropriate secondary
577 antibody conjugated to horse radish peroxidase (1:10,000, 5% w/v skim milk in TBST) for 1 h.
578 Membranes were washed in TBST and antibodies were detected by enhanced chemiluminescence
579 (Clarity Western ECL substrate, Bio-Rad Laboratories, Sydney NSW, Australia, or SuperSignal West
580 Femto Maximum Sensitivity Substrate, ThermoFisher Scientific) and imaged using a ChemiDoc
581 imaging system (Bio-Rad Laboratories). Densitometry was performed using Image Lab v6.1 (Bio-Rad
582 Laboratories) and normalised to the mean of the control group.

583 **Hydrolysis and AMP derivatisation of fatty acids**

584 Lipids were extracted from adherent cells grown to near-confluency in 6 well plates using the procedure
585 described above with the addition of 20 nmol of methyl nonadecanoate (Merck Life Science) as an
586 internal standard. Following MTBE extraction of lipids, an aliquot was taken and hydrolysed in 0.6 M
587 KOH in 75% v/v methanol at 60ºC for 30 min. Samples were then cooled to room temperature and
588 neutralised with 25% v/v acetic acid. Water and *n*-hexane (3:2 v/v) were added separately and samples
589 were vortexed vigorously before being centrifuged at 2000 *x g* for 5 min. The upper phase containing
590 hydrolysed fatty acids was removed, and the aqueous phase was washed with a second volume of *n*-
591 hexane and combined. The combined organic phase was then dried under N_2 at 37°C. Dried hydrolysed
592 fatty acids were derivatised with an AMP+ MaxSpec kit (Cayman Chemical, Ann Arbor, MI, USA) as
593 per manufacturer instructions [86]. Following this, AMP-derivatised fatty acids were re-extracted using
594 MTBE:water (1:1 v/v), and the upper MTBE phase was dried under N_2 before being resuspended in
595 methanol. Samples were stored at -20°C until analysis. A 37-component fatty acid methyl ester standard
596 (Merck Life Sciences) containing an additional 3.184 nmol of methyl nonadecanoate was concurrently
597 subjected to the same derivatisation procedure and used as an external quality control for fatty acid
598 identification by LC-MS. Derivatised MUFA standards FA 16:1*n*-9,*cis*, FA 16:1*n*-10,*cis*, FA 18:1*n*-

599 7,*cis*, FA 18:1*n*-10,*cis*, and FA 18:1*n*-12,*cis* were also spiked into this mixture to generate retention
600 times (RT) for MUFA isomer identification by LC-MS.

601 **OzFAD analysis of AMP-derivatised fatty acids**

602 Ozone-enabled fatty acid discovery analysis was conducted as previously described [37]. Briefly, 10 µL
603 injections of AMP+ derivatized fatty acids were subjected to reversed-phase chromatography using a
604 Waters ACQUITY Class UPLC (Waters Corporation, Milford, USA) fitted with an ACQUITY C18
605 reversed-phase column (2.1 × 100 mm i.d., particle size 1.7 µm, Waters Corporation) maintained at 60
606 °C. The 20 min gradient utilised a binary mobile phase system comprised A: water (0.1% formic acid)
607 and B: acetonitrile (0.1% formic acid). Chromatographic detection was conducted using an ion-mobility
608 enabled quadrupole time of flight (QTOF) mass spectrometer (SYNAPT G2-S*i* HDMS, Waters
609 Corporation) previously modified to allow introduction of high concentration ozone into the ion
610 mobility region of the instrument [87]. Electrospray ionisation parameters were: capillary +3 kV, sampling
611 cone +40 V, source temperature 120 °C, desolvation temperature 550 °C, cone gas 100 L/h, desolvation
612 gas 900 L/h, and nebulizer gas pressure 6.5 bar. Gas flows to the ion mobility region of the instrument
613 were 2.0, 180 and 90 mL/min, for the trap, helium cell and IMS region, respectively. For the ozonolysis
614 reactions, oxygen (≥ 99.999%, Coregas, NSW, Australia) was converted to ozone at concentrations of
615 220-240 g/Nm^3 (~15-17% O_3 in O_2) using a high concentration ozone generator (TG-40, Ozone
616 Solutions, Hull, IA). Peak areas for Criegee and aldehyde ions for each monounsaturated fatty acid
617 isomer were combined and normalised to internal standard and total protein (measured by BCA assay).

618 **Desaturase activity determination**

619 Cells were seeded in 6 well plates at a density of 3×10^5 cells/well and allowed to adhere overnight. The
620 following day, cell culture media was changed to FCS-free high glucose DMEM containing 12.5 µM
621 $^{13}C_{16}$-labelled or unlabelled palmitate conjugated to 2% fatty acid-free BSA. Palmitate was prepared in
622 cell culture media from 100 mM ethanolic stocks of palmitic acid and conjugated to fatty acid-free BSA
623 by incubating at 55 °C in media for 2 h. Lipids were extracted and derivatised as described above after
624 72 h of incubation with labelled or unlabelled palmitate. Lipids were identified and analysed as
625 described below for LC-MS analysis of AMP-derivatised fatty acids, with labelled fatty acids identified
626 from $[M+H+16.0542]^+$ precursors with the same RT as their unlabelled counterparts as per Table S3.

627 **LC-MS analysis of AMP-derivatised fatty acids**

628 AMP-derivatised fatty acids were separated on a core-shell C30 reverse phase column (Accucore 2.6
629 µm, 2.1 x 150 mm, ThermoFisher Scientific) on an Agilent 1290 Infinity II HPLC pump (Agilent
630 Technologies Inc, Santa Clara, CA, USA) using a modified gradient to that described above for OzFAD
631 analysis. Mobile phase A consisted of water and mobile phase B of acetonitrile (both containing 0.1%
632 formic acid), the flow rate was set at 0.4 mL/min throughout and the column heater at 30°C. The

633 gradient was as follows: 0-3.25 min increase from 50% B to 56% B, 3.25-6.5 min increase to 58% B,
634 6.5-7.5 min increase to 80% B, 7.5-9.5 min increase to 100% B, hold at 100% B for 1.5 mins. The
635 column was then re-equilibrated at 50% B for 4.5 mins. AMP-derivatised fatty acids were detected as
636 positive ions in QTOF-only mode on an Agilent 6560 IM-MS QTOF mass spectrometer (Agilent
637 Technologies). Source conditions were as follows: capillary voltage of 3.5 kV, nozzle voltage of 1 kV
638 and fragmentor at 360 V. Nitrogen was used as the sheath and collision gas, with drying gas set at 5
639 L/min and sheath gas at 12 L/min (both gases heated to 300°C) and the nebuliser pressure set at 20 psi.
640 Ions were acquired in Auto MS/MS mode at an MS1 mass range of *m/z* 100-1000 and MS2 mass range
641 of *m/z* 50-600. Spectra were acquired in MS1 mode at 5 spectra/s and 200 ms/spectrum, and in MS2
642 mode at 10 spectra/s and 100 ms/spectrum. Precursor ions were isolated using a window of 1.3 Th,
643 acquisition time of 50 ms/spectra, and collision energy of 45 eV. Calibration mix A was infused
644 throughout and masses were automatically detected and corrected using a 100 ppm window and
645 minimum height of 1×10^3 counts to ensure 5 ppm mass accuracy, with *m/z* 121.050873 and 922.009798
646 used as reference ions. AMP-derivatised fatty acids as $[M+H]^+$ were aligned using Mass Profinder v10.0
647 (Agilent Technologies) with an RT tolerance of 0.5 min and MS1 tolerance of 10 ppm. Lipids were
648 identified using a custom personal compound database and library (PCDL) generated from the RT of
649 external quality control samples (Table S3) and MS/MS spectra were manually inspected to ensure
650 correct MUFA isomer identification. Using this method, FA 18:1 isomers were only partially separated
651 and so these data were not analysed further. Data were exported, blank subtracted and quantified from
652 internal standards before being normalised to total protein.

653 **Knockdown by small interfering RNA**

654 Knockdown experiments were performed in adherent cells grown in 6 well plates for 72 h. Cells were
655 seeded at $1\text{-}3\times10^5$ cells/well and allowed to adhere overnight. Cells were transfected with Silencer
656 Select siRNA targeting *ACACA* (s883), *FASN* (s5030), *SCD* (s12505,s12504) *FADS2* (s18025,s18023)
657 or negative control (Silencer Select Negative Control No. 1) using Lipofectamine RNAiMAX
658 transfection reagent as per the manufacturer's instructions (ThermoFisher Scientific).

659 **RNAseq dataset analysis**

660 uPDAC tumour RNAseq data previously published by Zhou et al. [41] were used in this analysis. Genes
661 of interest (*ACACA*, *FASN*, *SCD*, *FADS2*) were filtered from the main dataset, alongside patients who
662 received either neo-adjuvant (Neoadj, n=9) or adjuvant (chemo-naïve, n=66) gemcitabine/nab-
663 paclitaxel treatment. Normalised counts were compared between the groups by unpaired t-test ($p <$
664 0.05).

665 **Statistical analysis**

666 Unless otherwise stated, all data were analysed by comparing CON with GEMR or CombAT cell lines
667 using an unpaired t-test with statistical significance set at $P < 0.05$. Data are expressed as means ±
668 standard error of the mean (SEM).

669 ## Acknowledgements

670 The authors acknowledge the use of the UNSW Sydney Mark Wainwright Bioanalytical Mass
671 Spectrometry Facility, QUT Central Analytical Research Facility, and Victor Chang Cardiac Research
672 Institute Innovation Centre Metabolomics & Microimaging Facilities (funded by the New South Wales
673 Government Ministry of Health) in this work. The authors also acknowledge and are grateful for input
674 on the project from cancer consumers Louise Bailey & Sundus Javed.

675 ## Funding sources

676 This project was supported by a Young Investigator Priority-driven Collaborative Cancer Research
677 Grant (APP1160909, funded by Cure Cancer Australia and Can Too!) awarded to SEH, a Miltenyi
678 Research Award (2022) & Victor Chang Cardiac Research Institute Outstanding Early and Mid-career
679 Researcher Grant award to OC, and a PanKind Accelerator grant awarded to NT, SEH, and SJB. BLJP
680 and SJB acknowledge support for enabling technologies from the Australian Research Council
681 Discovery (DP190101486) and Linkage Project (LP180100238).

682 ## Data availability

683 Analysis and raw files are available for all mass spectrometry data on Metabolomics Workbench,
684 including untargeted lipidomics for Panc1 (ST003757) GEMR, MiaPaCa2 (ST003758) GEMR, & both
685 CombAT cell lines (ST003760); fatty acids analysis for uniformly 13C palmitate-labelled cells
686 (ST003762), CombAT cells (ST003761) & siRNA knockdown (ST003763); and OzFAD data for
687 GEMR cell lines (ST003764).

688 ## Conflicts of Interest

689 The authors have no conflict of interest to declare.

690 ## References

691 1. Sung, H. *et al.* Global Cancer Statistics 2020: GLOBOCAN Estimates of Incidence and Mortality
692 Worldwide for 36 Cancers in 185 Countries. *CA. Cancer J. Clin.* **71**, 209–249 (2021).
693 2. Rawla, P., Sunkara, T. & Gaduputi, V. Epidemiology of Pancreatic Cancer: Global Trends,
694 Etiology and Risk Factors. *World J. Oncol.* **10**, 10–27 (2019).
695 3. Kleeff, J. *et al.* Pancreatic cancer. *Nat. Rev. Dis. Primer* **2**, 1–22 (2016).
696 4. Conroy, T. *et al.* FOLFIRINOX versus Gemcitabine for Metastatic Pancreatic Cancer. *N. Engl. J.*
697 *Med.* **364**, 1817–1825 (2011).
698 5. Chun, J. W. *et al.* Comparison between FOLFIRINOX and gemcitabine plus nab-paclitaxel
699 including sequential treatment for metastatic pancreatic cancer: a propensity score matching
700 approach. *BMC Cancer* **21**, 537 (2021).
701 6. Tempero, M. A. *et al.* Adjuvant nab-Paclitaxel + Gemcitabine in Resected Pancreatic Ductal
702 Adenocarcinoma: Results From a Randomized, Open-Label, Phase III Trial. *J. Clin. Oncol. Off. J.*
703 *Am. Soc. Clin. Oncol.* JCO2201134 (2022) doi:10.1200/JCO.22.01134.
704 7. Bailey, P. *et al.* Genomic analyses identify molecular subtypes of pancreatic cancer. *Nature* **531**,
705 47–52 (2016).
706 8. Jones, S. *et al.* Core signaling pathways in human pancreatic cancers revealed by global genomic
707 analyses. *Science* **321**, 1801–1806 (2008).
708 9. Hezel, A. F., Kimmelman, A. C., Stanger, B. Z., Bardeesy, N. & DePinho, R. A. Genetics and
709 biology of pancreatic ductal adenocarcinoma. *Genes Dev.* **20**, 1218–1249 (2006).
710 10. Liu, Y.-H., Hu, C.-M., Hsu, Y.-S. & Lee, W.-H. Interplays of glucose metabolism and KRAS
711 mutation in pancreatic ductal adenocarcinoma. *Cell Death Dis.* **13**, 1–10 (2022).
712 11. Yao, W., Maitra, A. & Ying, H. Recent insights into the biology of pancreatic cancer.
713 *EBioMedicine* **53**, 102655 (2020).
714 12. Myo Min, K. K. *et al.* Overcoming the Fibrotic Fortress in Pancreatic Ductal Adenocarcinoma:
715 Challenges and Opportunities. *Cancers* **15**, 2354 (2023).

716 13. Hardie, R.-A. *et al.* Mitochondrial mutations and metabolic adaptation in pancreatic cancer. *Cancer*
717 *Metab.* **5**, 2 (2017).
718 14. Gatto, F., Schulze, A. & Nielsen, J. Systematic Analysis Reveals that Cancer Mutations Converge
719 on Deregulated Metabolism of Arachidonate and Xenobiotics. *Cell Rep.* **16**, 878–895 (2016).
720 15. Kaoutari, A. E. *et al.* Metabolomic profiling of pancreatic adenocarcinoma reveals key features
721 driving clinical outcome and drug resistance. *EBioMedicine* **66**, 103332 (2021).
722 16. Wu, C. *et al.* Assessment of stromal SCD-induced drug resistance of PDAC using 3D-printed zPDX
723 model chips. *iScience* **26**, 105723 (2022).
724 17. Tadros, S. *et al.* De Novo Lipid Synthesis Facilitates Gemcitabine Resistance through Endoplasmic
725 Reticulum Stress in Pancreatic Cancer. *Cancer Res.* **77**, 5503–5517 (2017).
726 18. Sunami, Y., Rebelo, A. & Kleeff, J. Lipid Metabolism and Lipid Droplets in Pancreatic Cancer and
727 Stellate Cells. *Cancers* **10**, 3 (2017).
728 19. Rozeveld, C. N., Johnson, K. M., Zhang, L. & Razidlo, G. L. KRAS Controls Pancreatic Cancer
729 Cell Lipid Metabolism and Invasive Potential through the Lipase HSL. *Cancer Res.* **80**, 4932–4945
730 (2020).
731 20. Wang, G. *et al.* Metabolic detection and systems analyses of pancreatic ductal adenocarcinoma
732 through machine learning, lipidomics, and multi-omics. *Sci. Adv.* **7**, eabh2724 (2021).
733 21. Auciello, F. R. *et al.* A Stromal Lysolipid–Autotaxin Signaling Axis Promotes Pancreatic Tumor
734 Progression. *Cancer Discov.* **9**, 617–627 (2019).
735 22. Broadfield, L. A., Pane, A. A., Talebi, A., Swinnen, J. V. & Fendt, S.-M. Lipid metabolism in
736 cancer: New perspectives and emerging mechanisms. *Dev. Cell* **56**, 1363–1393 (2021).
737 23. Fhu, C. W. & Ali, A. Fatty Acid Synthase: An Emerging Target in Cancer. *Molecules* **25**, 3935
738 (2020).
739 24. Kuhajda, F. P. Fatty-acid synthase and human cancer: new perspectives on its role in tumor biology.
740 *Nutrition* **16**, 202–208 (2000).
741 25. Vanauberg, D., Schulz, C. & Lefebvre, T. Involvement of the pro-oncogenic enzyme fatty acid
742 synthase in the hallmarks of cancer: a promising target in anti-cancer therapies. *Oncogenesis* **12**,
743 1–10 (2023).

744 26. Yuan, Y. *et al.* Expression and prognostic significance of fatty acid synthase in clear cell renal cell
745 carcinoma. *Pathol. - Res. Pract.* **216**, 153227 (2020).
746 27. Yang, Y. *et al.* Role of fatty acid synthase in gemcitabine and radiation resistance of pancreatic
747 cancers. *Int. J. Biochem. Mol. Biol.* **2**, 89–98 (2011).
748 28. Ghaeidamini Harouni, M., Rahgozar, S., Rahimi Babasheikhali, S., Safavi, A. & Ghodousi, E. S.
749 Fatty acid synthase, a novel poor prognostic factor for acute lymphoblastic leukemia which can be
750 targeted by ginger extract. *Sci. Rep.* **10**, 14072 (2020).
751 29. Liu, H. *et al.* Fatty acid synthase causes drug resistance by inhibiting TNF-α and ceramide
752 production[S]. *J. Lipid Res.* **54**, 776–785 (2013).
753 30. Suzuki, T. *et al.* The biological role of metabolic reprogramming in pancreatic cancer. *MedComm*
754 **1**, 302–310 (2020).
755 31. Daemen, A. *et al.* Metabolite profiling stratifies pancreatic ductal adenocarcinomas into subtypes
756 with distinct sensitivities to metabolic inhibitors. *Proc. Natl. Acad. Sci.* **112**, E4410–E4417 (2015).
757 32. Chen, C. *et al.* Gemcitabine resistance of pancreatic cancer cells is mediated by IGF1R dependent
758 upregulation of CD44 expression and isoform switching. *Cell Death Dis.* **13**, 1–13 (2022).
759 33. El Amrani, M. *et al.* Gemcitabine-induced epithelial-mesenchymal transition-like changes sustain
760 chemoresistance of pancreatic cancer cells of mesenchymal-like phenotype. *Mol. Carcinog.* **58**,
761 1985–1997 (2019).
762 34. Wang, R. *et al.* Gemcitabine resistance is associated with epithelial-mesenchymal transition and
763 induction of HIF-1α in pancreatic cancer cells. *Curr. Cancer Drug Targets* **14**, 407–417 (2014).
764 35. Young, R. S. E. *et al.* Apocryphal FADS2 activity promotes fatty acid diversification in cancer.
765 *Cell Rep.* **34**, (2021).
766 36. Vriens, K. *et al.* Evidence for an alternative fatty acid desaturation pathway increasing cancer
767 plasticity. *Nature* 1 (2019) doi:10.1038/s41586-019-0904-1.
768 37. Menzel, J. P. *et al.* Ozone-enabled fatty acid discovery reveals unexpected diversity in the human
769 lipidome. *Nat. Commun.* **14**, 3940 (2023).
770 38. Garajová, I., Peroni, M., Gelsomino, F. & Leonardi, F. A Simple Overview of Pancreatic Cancer
771 Treatment for Clinical Oncologists. *Curr. Oncol.* **30**, 9587–9601 (2023).

772 39. Ueno, H. *et al.* Phase I/II study of nab-paclitaxel plus gemcitabine for chemotherapy-naive
773 Japanese patients with metastatic pancreatic cancer. *Cancer Chemother. Pharmacol.* **77**, 595–603
774 (2016).
775 40. Von Hoff, D. D. *et al.* Increased Survival in Pancreatic Cancer with nab-Paclitaxel plus
776 Gemcitabine. *N. Engl. J. Med.* **369**, 1691–1703 (2013).
777 41. Zhou, X. *et al.* Persister cell phenotypes contribute to poor patient outcomes after neoadjuvant
778 chemotherapy in PDAC. *Nat. Cancer* **4**, 1362–1381 (2023).
779 42. Walter, K. *et al.* Serum Fatty Acid Synthase as a Marker of Pancreatic Neoplasia. *Cancer*
780 *Epidemiol. Biomarkers Prev.* **18**, 2380–2385 (2009).
781 43. Han, L. *et al.* Enhanced De Novo Lipid Synthesis Mediated by FASN Induces Chemoresistance in
782 Colorectal Cancer. *Cancers* **15**, 562 (2023).
783 44. Ahmad, F. A. & Mahmud, S. Acute Pancreatitis Following Orlistat Therapy: Report of Two Cases.
784 *J. Pancreas* **11**, 0–0.
785 45. Bauerschlag, D. O. *et al.* Fatty acid synthase overexpression: target for therapy and reversal of
786 chemoresistance in ovarian cancer. *J. Transl. Med.* **13**, 146 (2015).
787 46. Al-Bahlani, S. *et al.* Fatty acid synthase regulates the chemosensitivity of breast cancer cells to
788 cisplatin-induced apoptosis. *Apoptosis* **22**, 865–876 (2017).
789 47. Souchek, J. J. *et al.* Fatty Acid Synthase Inhibitors Enhance Microtubule-Stabilizing and
790 Microtubule-Destabilizing Drugs in Taxane-Resistant Prostate Cancer Cells. *ACS Pharmacol.*
791 *Transl. Sci.* **6**, 1859–1869 (2023).
792 48. Bartolacci, C. *et al.* Targeting de novo lipogenesis and the Lands cycle induces ferroptosis in
793 KRAS-mutant lung cancer. *Nat. Commun.* **13**, 4327 (2022).
794 49. She, K. *et al.* SCD1 is required for EGFR-targeting cancer therapy of lung cancer via re-activation
795 of EGFR/PI3K/AKT signals. *Cancer Cell Int.* **19**, 1–11 (2019).
796 50. Tracz-Gaszewska, Z. & Dobrzyn, P. Stearoyl-CoA Desaturase 1 as a Therapeutic Target for the
797 Treatment of Cancer. *Cancers* **11**, 948 (2019).
798 51. Tissue expression of SCD - Summary - The Human Protein Atlas.
799 https://www.proteinatlas.org/ENSG00000099194-SCD/tissue.

800 52. Skrypek, K., Balog, S., Eriguchi, Y. & Asahina, K. Inhibition of Stearoyl-CoA Desaturase Induces
801 the Unfolded Protein Response in Pancreatic Tumors and Suppresses Their Growth. *Pancreas* **50**,
802 219–226 (2021).
803 53. Li, Y.-L., Tian, H., Jiang, J., Zhang, Y. & Qi, X.-W. Multifaceted regulation and functions of fatty
804 acid desaturase 2 in human cancers. *Am. J. Cancer Res.* **10**, 4098–4111 (2020).
805 54. Xuan, Y. *et al.* SCD1/FADS2 fatty acid desaturases equipoise lipid metabolic activity and redox-
806 driven ferroptosis in ascites-derived ovarian cancer cells. *Theranostics* **12**, 3534–3552 (2022).
807 55. Wang, J. *et al.* Delta-6-desaturase inhibitor enhances radiation therapy in glioblastoma in vitro and
808 in vivo. *Cancer Manag. Res.* **10**, 6779–6790 (2018).
809 56. He, C. *et al.* Inhibiting Delta-6 Desaturase Activity Suppresses Tumor Growth in Mice. *PLOS ONE*
810 **7**, e47567 (2012).
811 57. Hasegawa, K. *et al.* Delta-6 desaturase FADS2 is a tumor-promoting factor in cholangiocarcinoma.
812 *Cancer Sci.* (2024) doi:10.1111/cas.16306.
813 58. Hansen-Petrik, M. B. *et al.* Selective inhibition of Δ-6 desaturase impedes intestinal tumorigenesis.
814 *Cancer Lett.* **175**, 157–163 (2002).
815 59. Ikeda, T. *et al.* FADS2 confers SCD1 inhibition resistance to cancer cells by modulating the ER
816 stress response. *Sci. Rep.* **14**, 13116 (2024).
817 60. Vockley, J. Optimizing metabolism is a complex issue. *Nat. Metab.* 1–2 (2024)
818 doi:10.1038/s42255-023-00965-x.
819 61. Fischer, E. & Sauer, U. Large-scale in vivo flux analysis shows rigidity and suboptimal
820 performance of Bacillus subtilis metabolism. *Nat. Genet.* **37**, 636–640 (2005).
821 62. Qin, C. *et al.* Metabolism of pancreatic cancer: paving the way to better anticancer strategies. *Mol.*
822 *Cancer* **19**, 50 (2020).
823 63. Cerone, M. & Smith, T. K. Desaturases: Structural and mechanistic insights into the biosynthesis
824 of unsaturated fatty acids. *Iubmb Life* **74**, 1036–1051 (2022).
825 64. Son, J. *et al.* Glutamine supports pancreatic cancer growth through a KRAS-regulated metabolic
826 pathway. *Nature* **496**, 101–105 (2013).

827 65. Piccolis, M. *et al.* Probing the Global Cellular Responses to Lipotoxicity Caused by Saturated Fatty
828 Acids. *Mol. Cell* **74**, 32-44.e8 (2019).
829 66. Sánchez-Martínez, R. *et al.* A link between lipid metabolism and epithelial-mesenchymal transition
830 provides a target for colon cancer therapy. *Oncotarget* **6**, 38719–38736 (2015).
831 67. Giudetti, A. M. *et al.* A specific lipid metabolic profile is associated with the epithelial
832 mesenchymal transition program. *Biochim. Biophys. Acta BBA - Mol. Cell Biol. Lipids* **1864**, 344–
833 357 (2019).
834 68. Lee, H. J. *et al.* Multimodal Metabolic Imaging Reveals Pigment Reduction and Lipid
835 Accumulation in Metastatic Melanoma. *BME Front.* **2021**, 9860123.
836 69. Schwab, A. *et al.* Zeb1 mediates EMT/plasticity-associated ferroptosis sensitivity in cancer cells
837 by regulating lipogenic enzyme expression and phospholipid composition. *Nat. Cell Biol.* 1–12
838 (2024) doi:10.1038/s41556-024-01464-1.
839 70. Afanas'ev, I. Reactive Oxygen Species Signaling in Cancer: Comparison with Aging. *Aging Dis.*
840 **2**, 219–230 (2010).
841 71. Abdel Hadi, N., Reyes-Castellanos, G. & Carrier, A. Targeting Redox Metabolism in Pancreatic
842 Cancer. *Int. J. Mol. Sci.* **22**, 1534 (2021).
843 72. Magtanong, L. *et al.* Exogenous Monounsaturated Fatty Acids Promote a Ferroptosis-Resistant
844 Cell State. *Cell Chem. Biol.* **26**, 420-432.e9 (2019).
845 73. Tesfay, L. *et al.* Steroyl-CoA Desaturase 1 (SCD1) protects ovarian cancer cells from ferroptotic
846 cell death. *Cancer Res.* **79**, 5355–5366 (2019).
847 74. Liu, G., Yang, D., Meng, J., He, Q. & Wu, D. The combination of gemcitabine and albumin-bound
848 paclitaxel effectively inhibits de novo lipogenesis in pancreatic cancer cells by targeting the
849 AMPK/SREBP1 pathway. *Biochem. Pharmacol.* **232**, 116721 (2025).
850 75. Zheng, W. & Xu, S. Analysis of Differential Expression Proteins of Paclitaxel-Treated Lung
851 Adenocarcinoma Cell A549 Using Tandem Mass Tag-Based Quantitative Proteomics.
852 *OncoTargets Ther.* **13**, 10297–10313 (2020).

853 76. Guillou, H., Martin, P. G. P. & Pineau, T. Transcriptional Regulation of Hepatic Fatty Acid
854 Metabolism. in *Lipids in Health and Disease* (eds. Quinn, P. J. & Wang, X.) 3–47 (Springer
855 Netherlands, Dordrecht, 2008). doi:10.1007/978-1-4020-8831-5_1.
856 77. Triki, M. *et al.* mTOR Signaling and SREBP Activity Increase FADS2 Expression and Can
857 Activate Sapienate Biosynthesis. *Cell Rep.* **31**, 107806 (2020).
858 78. Abbott, S. K. *et al.* An Improved High-Throughput Lipid Extraction Method for the Analysis of
859 Human Brain. *Lipids* **48**, 307–318 (2013).
860 79. Norris, S. E., Friedrich, M. G., Mitchell, T. W., Truscott, R. J. W. & Else, P. L. Human prefrontal
861 cortex phospholipids containing docosahexaenoic acid increase during normal adult aging, whereas
862 those containing arachidonic acid decrease. *Neurobiol. Aging* **36**, 1659–69 (2015).
863 80. Jayashankar, V. *et al.* Drug-like sphingolipid SH-BC-893 opposes ceramide-induced mitochondrial
864 fission and corrects diet-induced obesity. *EMBO Mol. Med.* e13086 (2021)
865 doi:10.15252/emmm.202013086.
866 81. Hu, C. *et al.* RPLC-Ion-Trap-FTMS Method for Lipid Profiling of Plasma: Method Validation and
867 Application to p53 Mutant Mouse Model. *J. Proteome Res.* **7**, 4982–4991 (2008).
868 82. Bird, S. S., Marur, V. R., Sniatynski, M. J., Greenberg, H. K. & Kristal, B. S. Serum Lipidomics
869 Profiling Using LC–MS and High-Energy Collisional Dissociation Fragmentation: Focus on
870 Triglyceride Detection and Characterization. *Anal. Chem.* **83**, 6648–6657 (2011).
871 83. Turner, N. *et al.* A selective inhibitor of ceramide synthase 1 reveals a novel role in fat metabolism.
872 *Nat. Commun.* **9**, 3165 (2018).
873 84. Tsugawa, H. *et al.* MS-DIAL: data-independent MS/MS deconvolution for comprehensive
874 metabolome analysis. *Nat. Methods* **12**, 523–526 (2015).
875 85. Folch, J., Lees, M. & Sloane Stanley, G. H. A simple method for the isolation and purification of
876 total lipides from animal tissues. *J. Biol. Chem.* **226**, 497–509 (1957).
877 86. Bollinger, J. G. *et al.* Improved Sensitivity Mass Spectrometric Detection of Eicosanoids by Charge
878 Reversal Derivatization. *Anal. Chem.* **82**, 6790–6796 (2010).
879 87. Poad, B. L. J. *et al.* High-Pressure Ozone-Induced Dissociation for Lipid Structure Elucidation on
880 Fast Chromatographic Timescales. *Anal. Chem.* **89**, 4223–4229 (2017).